Improved photocatalytic performance of ZnO nanograss decorated pore-array films by surface texture modification and silver nanoparticle deposition

Shao-Tsu Hung, Chi-Jung Chang*, Mu-Hsiang Hsu

Department of Chemical Engineering, Feng Chia University, 100 Wenhwa Road, Seatwen, Taichung 40724, Taiwan, ROC

ABSTRACT

Immobilized photocatalyst was prepared by the growth of ZnO nanograss on the ZnO pore-array substrate. The surface morphology, optical and photocatalytic properties of the photocatalysts were studied. Nanograss decorated ZnO pore-array films exhibited improved performance on the photocatalytic degradation of methyl orange (MO) in aqueous solution under UV radiation. The photocatalytic activity of pore-array films can be tuned by changing the surface nanostructure of the porous photocatalyst. The enhanced photocatalytic activity of the nanostructured pore-array photocatalyst can be attributed to increased active surface area, improved diffusion of dye molecules among the nanostructured catalyst, and enhanced light absorption through the light-trapping effect. Besides, the degradation of MO using Ag/ZnO composite pore-array catalysts with different sizes and densities of the Ag particles on the surface of ZnO nanostructure was investigated.

© 2011 Elsevier B.V. All rights reserved.

1. Introduction

The removal of dyes and toxic organic compounds from wastewater has been studied widely and has attracted more attention as cleaner and greener technology. Semiconductor-assisted photocatalysis can be used for large-scale purification of wastewaters at low cost. Semiconductors such as TiO_2 and ZnO were used as photocatalysts because of their high photosensitivity, good long-term stability, and non-toxic nature [1]. The form of the photocatalyst has strong impacts on the photocatalytic performance and cost. Nanosized catalyst slurries have high solid to liquid contact areas which help to achieve high reaction rates in wastewater [2,3]. ZnO photocatalysts are often applied in the form of aqueous slurries. However, it may encounter technological problems including the particle aggregation, together with the need for the separation and recycling of the photocatalyst nanoparticles from the slurry after the wastewater treatment process. Recent investigations on photocatalysis are oriented toward the immobilization of photocatalyst as thin films on the support substrates [4,5]. Various materials of different shapes, such as glass fiber, glass bead, aluminum foil sheet, and plastic fiber-optic cable, have been proposed as catalyst support. However, compared with that of the corresponding nanoparticles suspensions, the efficiency of the immobilized thin film photocatalyst is lower because the active surface area of the thin film photocatalyst is dramatically reduced [6,7]. This problem can be solved by replacing the thin film photocatalyst with nanostructured photocatalyst, which possess more active sites and higher surface-to-volume ratio than the thin film analog.

Two-dimensional ordered pore-array films made of various materials have been fabricated by the nanosphere lithography method [8–10]. These films with ordered pore-array surfaces have large surface area [11] and exhibit unique properties such as UV-induced wettability transition [12,13] and enhanced thermal-responsive surfaces [14]. Ordered pore-array films have potential applications in catalysis [15], photonic crystals [16], gas sensors [17], and optical-electronic devices [18]. However, a comprehensive study of the nanograss decorated hemisphere pore-array ZnO film regarding its surface morphology, optical and photocatalytic properties has not been undertaken yet. Such research will enable further applications of nanostructured ZnO photocatalyst.

Photoexcitation of semiconductor oxide photocatalyst by UV light results in the generation of electron–hole pairs which enable the production of hydroxyl radicals in water. A major limitation of achieving high photocatalytic efficiency in the semiconductor photocatalyst is the rapid recombination of photo-induced charge carriers [19]. The charge separation efficiency can be improved by using semiconductor composite [20,21] or depositing metal nanoparticles on the semiconductor [22,23]. Deposition of noble metals on semiconductor photocatalysts can enhance their photocatalytic activities.

The aim of this study is to prepare immobilized ZnO photocatalysts with high performances. Our strategy includes the deposition of Ag nanoparticles on the photocatalyst surface and the modification of surface texture. The photocatalyst with the

---

* Corresponding author. Tel.: +886 4 24517250x3678; fax: +886 4 24510890.
  E-mail address: changcj@fcu.edu.tw (C.-J. Chang).

ZnO nanograss modified pore-array structures has been developed. After the growth of ZnO pore-array by the nanosphere lithography and electrochemical deposition methods, short ZnO nanorod were grown on the ZnO pore-array to fabricate the ZnO nanograss decorated pore-array films through a hydrothermal approach. The performance can be enhanced by increasing the surface area of the catalyst by introducing the three-dimensional ZnO nanostructure, enhancing the diffusion of dye molecules around the catalyst with hemisphere microporous surface, and increasing the absorption of light through the light-trapping effect. Photodegradation properties of methyl orange (MO) using these photocatalysts with various surface morphology were investigated. Besides, the enhancement of photocatalytic performance by depositing silver nanoparticles on the nanograss pore-array catalysts was also studied.

2. Experimental

2.1. Materials

Zinc acetate dihydrate and zinc nitrate 6-hydrate were provided by J.T.Baker. Hexadecyl trimethyl ammonium and sodium dodecyl sulfate were bought from TCI. Silver nitrate (SHOWA), hexamethylenetetramine (Riedel-de Haën), and methyl orange (Alfa Aesar) were used as received. HP hollow particle (Ropaque HP1055, Rohm and Haas, solid content: 26.7%, the hollow acrylic/styrene sphere dispersed in water) have been used as the template. The HP particle has an outer diameter of 800 nm and an inner pore diameter of 600 nm [24].

2.2. Preparation of photocatalysts

Fig. 1 shows the schematic illustration of the fabrication process of the ZnO nanograss decorated pore-array photocatalysts. The details are listed as follows.

2.2.1. Pore-array films

ZnO pore-array films were fabricated by the process including self-assembled polymeric hollow particles as the microsphere mask, growth of ZnO nanostructures in the interstice, and removal of the microsphere mask. Suspensions of anionic charged hollow acrylic/styrene spheres, were further diluted with D.I. water (weight ratio of suspension:water = 1:4). The diluted solution was dropped onto a cleaned ITO glass substrate, which was inclined about 40°. Then, the hollow acrylic/styrene sphere were floated at the air/water interface by slow immersion of the substrate into the aqueous solution with 1% surfactant (sodium dodecyl sulfate, SDS) under a shallow angle. The hollow spheres detached from the substrate, self-assembled in a dense monolayer, and remained afloat on the water surface. Then, the floating layer of colloidal spheres was picked up by another ITO glass substrate using a procedure which was the reverse of the immersion process. After the evaporation of the liquid, the hollow spheres were self-assembled into a homogenous, dense monolayer ordered nanosphere mask. The spheres were fixed on the ITO glass substrate by baking the substrate at 100 °C for 20 min. Then, ZnO was grown on the ITO glass substrates from the interstices of adjacent microspheres by electrochemical deposition (ECD) method in an aqueous solution composed of 0.1 M $Zn(NO_3)_2$ at 80 °C. ECD was carried out using a platinum plate as the counter electrode, ITO glass as the cathodic substrate and a SCE as a reference electrode. The samples were washed with D.I. water and then annealed at 450 °C for 2 h to remove the microsphere mask and make the ZnO pore-array films.
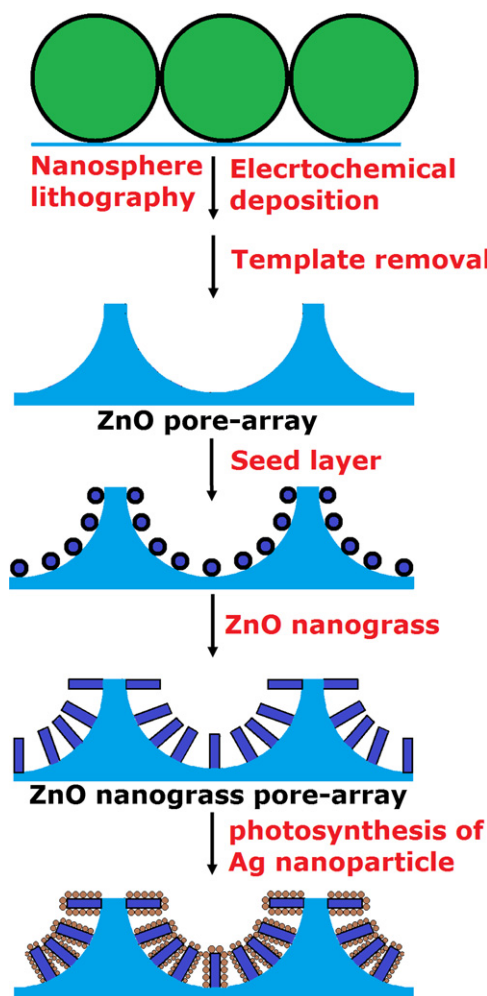

Fig. 1. Schematic illustrations of fabricating ZnO nanograss decorated pore-array films.

2.2.2. Flat ZnO film

The flat ZnO film was grown on the ITO glass by the electrochemical deposition method. The deposition time was 90 s. The deposition voltage was 1.2 V.

2.2.3. Nanograss decorated pore-array films

For the fabrication of seed solution, 0.1 M zinc acetate was dissolved in the ethanol at 60 °C. The solution was cooled to 0 °C. Then, n-hexadecyltrimethylammonium hydroxide (HTAOH) was added (Zn^{2+}/HTAOH = 1/2) and the solution was stirred for 30 min. The resulting mixture was then agitated at 60 °C for 2 h to yield a homogeneous and stable colloid solution, which served as the seed solution. The pore-array films were coated with the colloidal seed solution. Then they were dried and annealed at 300 °C for 1 h to make a seed layer on the pore-array substrates.

Then, the ZnO nanograss was grown on the surface of the pore-array films by immersing the substrates in the aqueous solution containing $Zn(NO_3)_2$ (0.05 M) and hexamethylene–tetramine (0.05 M) at 95 °C for different period of time (75, 90, and 105 min).

2.2.4. Silver nanoparticles decorated nanograss pore-array films

To examine the role of the Ag nanoparticles on the photocatalysis properties, photosynthesis of Ag nanoparticles on the ZnO nanorods has been preformed in silver nitrate solutions under 365-nm irradiation. A piece of ZnO nanograss pore-array film was immersed into the silver nitrate ($AgNO_3$) solution with

different concentration of silver precursor (10^{-3} M, 5×10^{-3} M, and 10^{-2} M) and was irradiated by 365-nm UV-light with an intensity of 14.3 mW/cm^2 for 30 min to make the Ag decorated films.

2.3. Characterization

XRD studies were carried out with a MAC SCIENCE MXP3 diffractometer. The morphology, energy dispersive X-ray (EDX) and Ag mapping measurements were conducted with a HITACHI S-4800 field emission scanning electron microscope (FESEM). The absorbance of the dye solution, the transmittance and reflectance of the catalyst film were measured by the PL 2006 mutifuntional spectrometer (Labguide Co.).

2.4. Photocatalytic degradations

ZnO nanograss decorated pore-array photocatalysts were added into a testing container with 10 mL MO aqueous solution (concentration is 15 mg/L). The MO solution was continuously stirred when the UV light (365 nm, 14.3 mW/cm^2) irradiation started. 3.5 mL MO aqueous solution about was withdrawn per 30 min to monitor the absorbance spectra. The degradation process was monitored by the UV–vis absorbance spectrometer (measuring the absorbance of MO at 463 nm). The UV light was turned off during the absorbance monitoring process. Then, 3.5 mL MO aqueous solution was poured into the testing container. The UV light irradiation toward the MO solution continued. The absorption spectra were recorded and the rate of decolorization was observed in terms of change in intensity at λ_{max} of the dyes. The decolorization efficiency (%) has been calculated as

$$\text{efficiency}(\%) = \frac{C_0 - C}{C_0} \times 100$$

where C_0 is the initial concentration of dye and C is the concentration of dye after irradiation of UV light.

2.5. Nomenclature of the samples

The nanograss decorated ZnO pore-array samples were identified as PAGxSy. The symbols G and PA represent ZnO nanograss decorated sample and ZnO pore-array film, respectively. x ($x = 1$, 2, and 3) means the ZnO nanograss growth time (75, 90, and 105 min). S represents the silver nanoparticle deposited sample. y ($y = 1$, 2, and 3) means the concentration of silver precursor (10^{-3} M, 5×10^{-3} M, and 10^{-2} M). PA means the pore-array samples without modification. PAGx represents the nanograss decorated pore-array samples without Ag nanoparticles decoration.

3. Results and discussion

Before the fabrication of ZnO pore-array films, polymeric hollow particles were self-assembled on the glass substrate to make the microsphere mask. The top-view FESEM image of self-assembled hollow spheres shown in Fig. 2 reveals the monolayer structure of the microsphere mask.

3.1. Analysis of porous structures

The surface textures of ZnO nanograss decorated pore-array (NGPA) films were tuned by changing the nanograss growth time. Fig. 3 shows the top-view FESEM images of the ZnO pore-array (PA) films and nanograss decorated pore-array films. The nanograss growth time for nanograss decorated pore-array films PAG1, PAG2, and PAG3 are 75 min, 90 min, and 105 min, respectively. Fig. 3(e)–(h) is higher magnification images of Fig. 3(a)–(d). The pores are orderly arranged in the PA film (Fig. 3a), which are
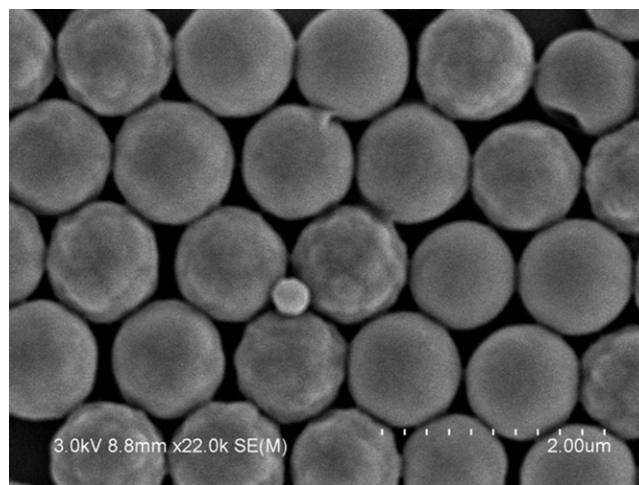

Fig. 2. Top-view FESEM image of self-assembled hollow spheres.

the reverse replica of the hollow sphere template. Hemisphere pores with circular wreath were observed. For the PAG1 sample (Fig. 3b), the ZnO nanorods (nanograss) are grown on the wreath and inside the pores. Hexagonally packed pore-array structure with thick edges was obtained. When the nanograss growth time was extended from 75 min (PAG1) to 105 min (PAG3, Fig. 3d), the thickness of the wreath increased because of increasing ZnO nanograss length. The diameter of the pore became smaller as the nanograss growth time got longer. Variations in pore diameters were observed between different pores, especially the PAG3 film.

The cross-sectional images of PA, PAG1, PAG2, and PAG3 films are shown in Fig. 4. The pores in the PA film (Fig. 4a) look like truncated hollow hemispheres. The cross-sectional images revealed that the depth of the pore is about 500 nm. The diameter of the pore is about 940 nm. After coating the seed solution, the ZnO nanograss was grown on the pore-array surfaces to modify the surface texture. The cross-sectional image of PAG1 (Fig. 4b) reveals that the nanograss is fabricated not only on the wreath (pore edge) but also on the hemisphere pore surface. The pore-edge skeleton composes of the ZnO nanograss. In order to maintain the structure of the nanograss during the sample cleavage procedure, the PAG1 sample was encapsulated by the epoxy resin in advance. However, Fig. 4b shows that some of the nanograss was covered by the epoxy resin. The PAG2 film was cleaved without polymer encapsulation in advance. Fig. 4c shows the cross-sectional image of the PAG2 film. Some of the nanograss collapse during the cleaving procedure. It revealed that the nanograss was grown inside the pore. Schematic illustration of the cross-sectional pore morphology of the ZnO nanograss decorated pore-array films was shown in Fig. 5. The porous structure of the nanograss decorated pore-array can be analyzed by measuring four parameters of the cross-sectional image. D and d represent the diameters of the pore and nanograss, respectively. L is the depth of the pore. H means the thickness of the pore bottom (including the nanograss). D and d were measured from the top-view images of the samples which were shown in Fig. 3. H and L were measured from the cross-sectional images of the samples (Fig. 4). The results of PAG1, PAG2, and PAG3 films are listed in Table 1. When the nanograss growth time of the film was extended from 75 min (PAG1) to 105 min (PAG3), the thickness of the wreath increased because of increasing ZnO nanograss length. The height of the pore wall and thickness of the bottom (H) also increase as the nanograss growth time increased. D decreases and d increases as the nanograss growth time increased. For the PAG1 sample, the
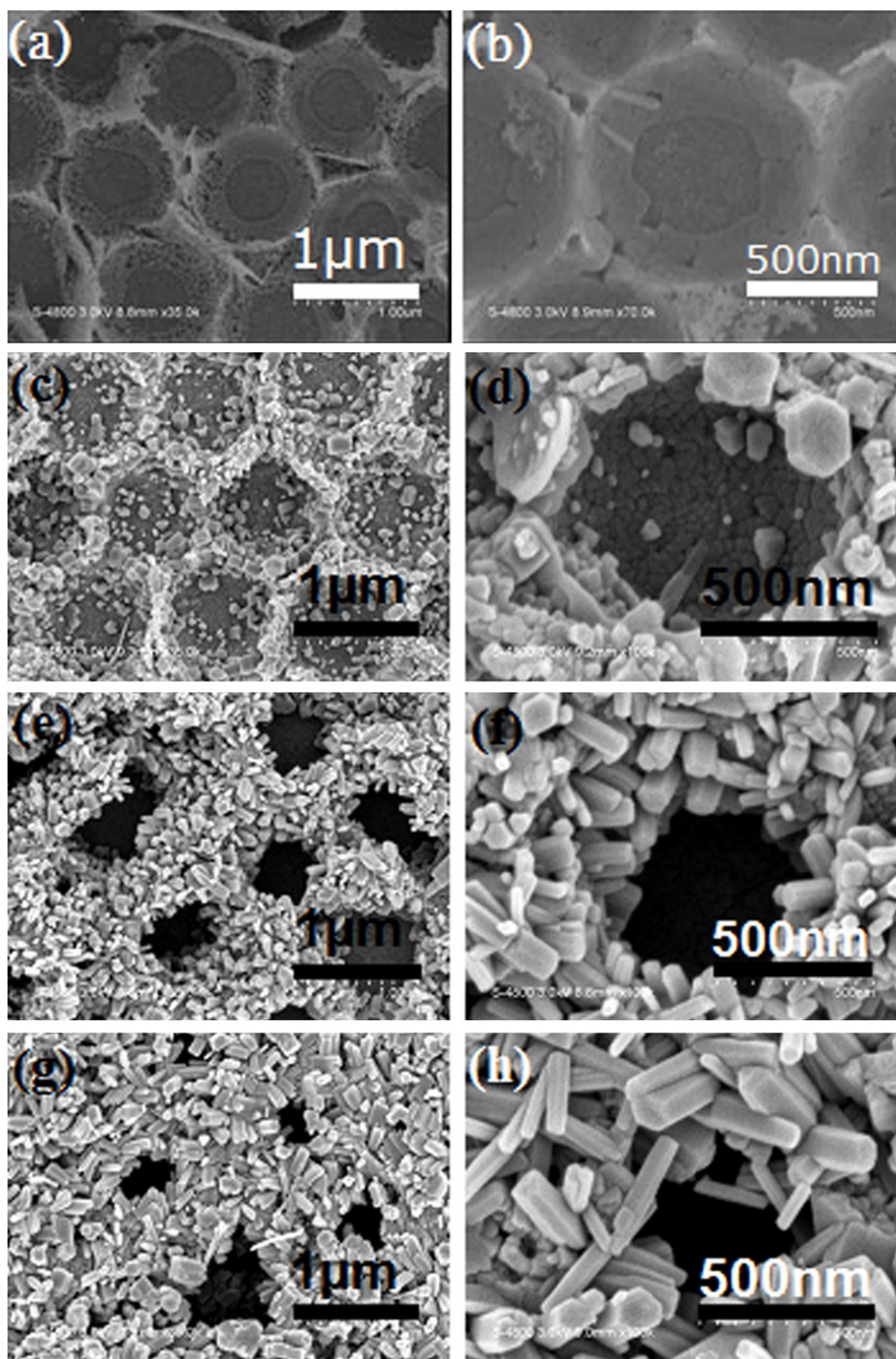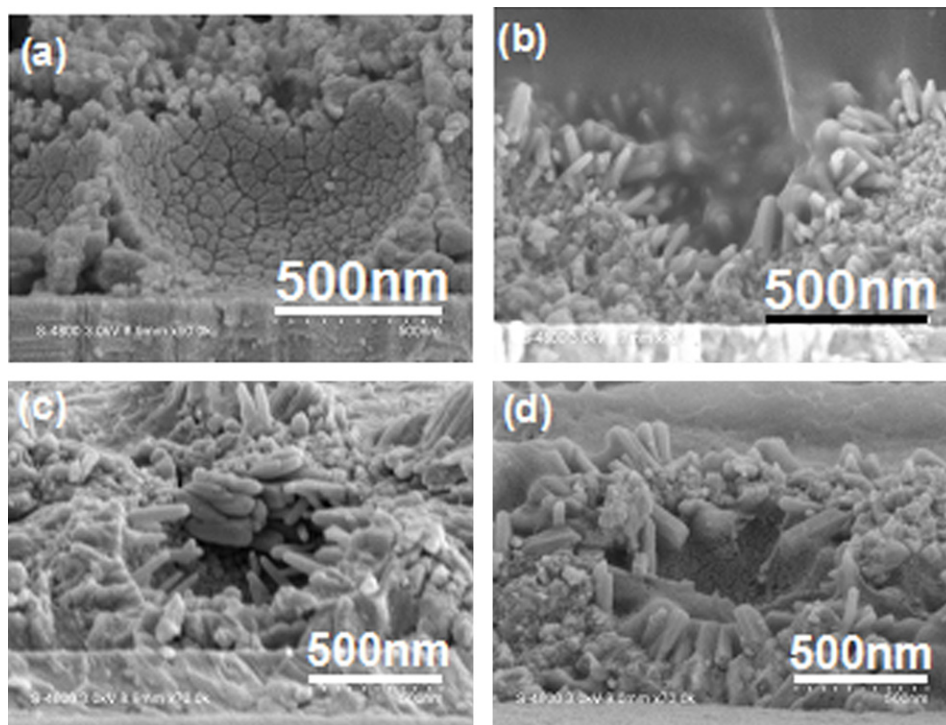
Fig. 3. Top-view FESEM images of the (a) ZnO pore-array films and nanograss decorated pore-array film with different nanograss growth time, (b) PAG1, 75 min, (c) PAG2, 90 min, and (d) PAG3, 105 min. (e–h) are higher magnification images of (a–d).

pore diameters (D) of different pores show good uniformity. However, as the nanograss growth time exceeds 90 min, D and d of the PAG2 (growth time = 90 min) and PAG3 (growth time = 105 min) samples exhibit considerable variations. The top view images show that the pore wreath is no longer circular. Extending the length of ZnO nanograss deteriorated the ordered pore-array structures. The pore structure will disappear when the nanograss growth time exceeds 120 min. The pore is completely filled by the ZnO nanograss.

3.2. XRD patterns

X-ray diffraction (XRD) was performed on ZnO pore-array substrates with and without decoration of nanograss. Fig. 6 shows the XRD patterns of (a) ZnO PA film (b) ZnO nanograss decorated pore-array PAG3 films in the range of 10–70° (2θ). The result in Fig. 6(a) indicates that ordered PA film is composed of polycrystalline zinc oxide. The XRD pattern of the ZnO pore-array film shows peaks which are indexed to (1 0 0), (0 0 2), (1 0 1), (1 0 2),

Fig. 4. Cross-sectional FESEM images of the (a) ZnO pore-array film and nanograss decorated pore-array films, (b) PAG1, (c) PAG2, and (d) PAG3.
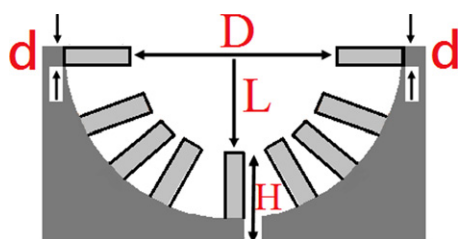
Fig. 5. Schematic illustrations of the cross-sectional pore morphology of the ZnO nanograss decorated pore-array films.

Table 1
Dimensional parameters of the nanograss decorated pore-array structure.

	d (nm)	H (nm)	L (nm)	D (nm)
PAG1	40–50	235	445	830
PAG2	50–75	215	440	440–580
PAG3	50–100	310	510	200–530

and (1 1 0) of wurtzite-structured ZnO. The (1 0 0) and (1 0 1) peaks are much larger than the other peaks. The XRD pattern of the ZnO nanograss (Fig. 6b) shows peaks which are indexed to (1 0 0), (0 0 2), (1 0 1), (1 0 2), and (1 1 0) of wurtzite-structured ZnO. The remarkably enhanced (0 0 2) diffraction peak is much more intensive than the other peaks, implying that the ZnO nanograss was grown along the *c*-axis. The nanograss oriented perpendicular to the pore-array surfaces. Since the ZnO nanostructure is built on the ITO glass substrate, there are some peaks which can be assigned as reflection lines of ITO. In Fig. 6a the diffraction peaks at $2\theta = 21.5°$, $36.0°$, and $50.5°$ are assigned as (2 1 1), (4 0 0), and (4 4 1) reflection lines of ITO. In Fig. 6b the diffraction peaks at $2\theta = 30.5°$ and $68.0°$ are assigned as (1 0 0) and (2 0 0) reflection lines of ITO.

3.3. Light trapping

To investigate the effect of surface morphology on the light-trapping performance, five ZnO films including pore-array (PA) films, nanograss decorated pore-array films (PAG1, PAG2, and PAG3), and flat ZnO film were prepared to check their optical properties. The reflectance and transmittance of (i) flat ZnO film, (ii) ZnO pore-array film and ZnO nanograss decorated pore-array photocatalysts, (iii) PAG1, (iv) PAG2, and (v) PAG3 are depicted in Fig. 7. The reflectance of the PA film was lower than that of the flat ZnO film.

The reflectance of the PA film is lower than that of the flat film. The reflectances of the PAGn series films are lower than that of the PA film, especially in the 300–330 nm and 450–700 nm range. The reflectance of the PAG3 film gets further lower as the nanograss growth time increased. The transmittance spectra revealed that the transmittances of PAGn and PA films were nearly the same in the UV range (wavelength: 300–400 nm). The growth of ZnO nanograss on the pore-array lowers the transmittance of the visible light (wavelength: 400–700 nm). Comparing the spectra of PAG1, PAG2, and PAG3 films, increasing length of the nanograss by extending the growth time resulted in the decrease in both the transmittance and reflectance. Formation of such texture is useful in fabricating photocatalyst which is operated under UV radiation or visible light. The geometry of the proposed light trapping scheme is shown in Fig. 8a. Incident optical rays bounce off the photocatalyst structure multiple times. This multiple scattering can produce a longer optical path length inside the porous ZnO films. The light absorption efficiency can be enhanced. Extending the length of nanograss on the pore-array surface helps to enhance the light trapping efficiency. Since the light-trapping effects of the PAGx series samples are strong in the visible-light range, such technique can be applied to the research of visible-light photocatalyst applications in the future.

Berginski et al. [25] showed that regularly distributed craters with mean opening angles between 120° and 135° and lateral sizes of 1–3 μm are very effective in light scattering. In this study, PAG3

Fig. 7. (a) Reflectance and (b) transmittance spectra of (i) flat ZnO film (ii) ZnO pore-array films and ZnO nanograss decorated pore-array films (iii) PAG1 (iv) PAG2 (v) PAG3.
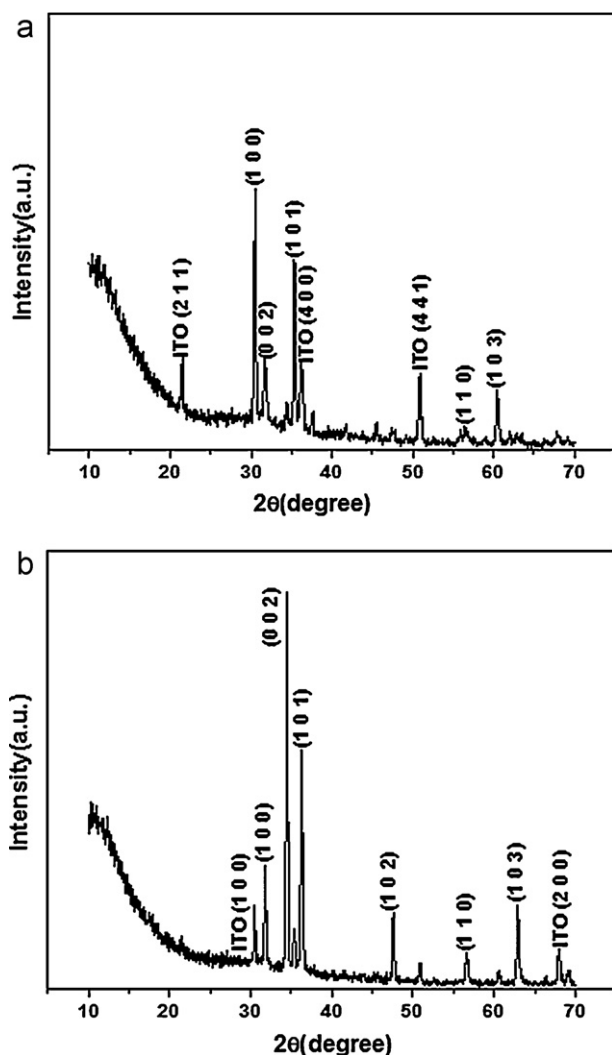
Fig. 6. XRD patterns of (a) ZnO pore-array films and (b) nanograss decorated pore-array PAG3 films (*peaks related to ITO).

pore-array films consists of pores with depth up to 510 nm and pore-diameter ranging from 200 nm to 500 nm. Besides, the diameter of the nanograss ranges from 50 to 100 nm. The interstics among the nanograss are less than 100 nm. Such kind of surface texture with microscale hemisphere pores and nanoscale interstics exhibited enhanced light trapping.

3.4. Photocatalytic performace

3.4.1. Catalyst loading and surface texture

The surface texture of the nanostructured photocatalyst has strong influences on the photocatalytic performance. The dye solution was continuously stirred during the photocatalytic degradation test. As shown in Fig. 8b, the diffusion of dye molecules toward the porous nanograss decorated pore-array photocatalysts consists of two steps. The first is the diffusion of dye molecules into the micropores. The second is the diffusion of dye molecules into the interstice of the nanograss.

The diffusion of dye molecules into the micropores is a process with small Knudsen number. The mean free path is small compared to the pore diameter. The diffusion can be predicted by Fick's law. The Knudsen number [26] is a dimensionless number defined as
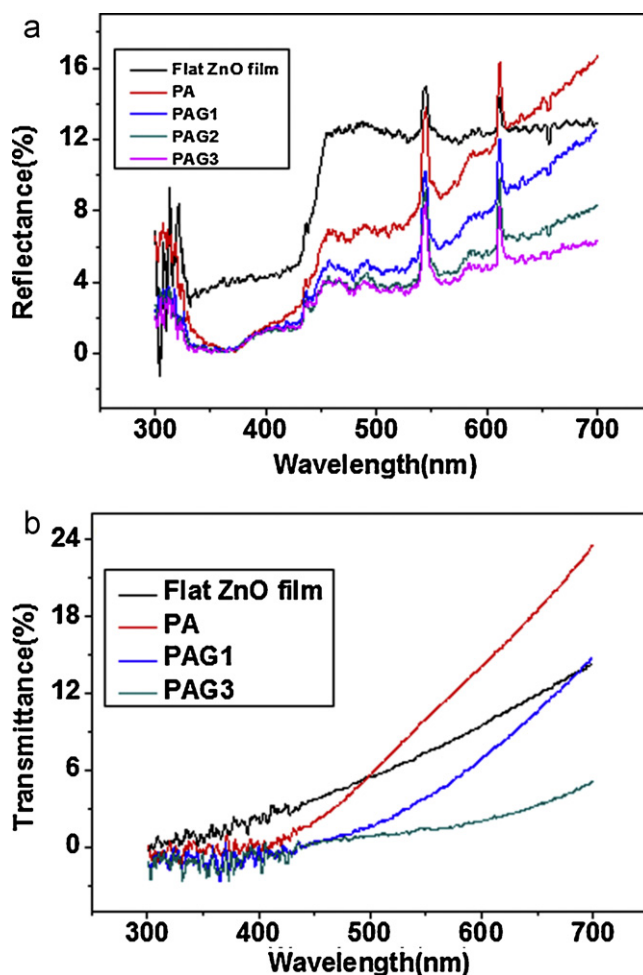
$$K_n = \frac{\lambda}{2r},$$

where λ is the mean free path and r is the average pore radius. The mean free path is the average distance covered by a moving dye particle between successive collisions which modify its direction or energy or other particle properties.

For the diffusion of dye molecules in the interstics of the nanograss which is a long pore with a narrow pore radius (<50 nm), the dye molecules colloids with the wall. The molecule–wall collisions are important. Diffusion of dye molecules among the nanograss is a Knudsen diffusion which describes the movement of fluids with a high Knudsen number. The mean free path of a molecule is larger than the average pore radius. The diffusivity is calculated using modified Knudsen diffusion model [26]. The diffusivity is expressed as follows

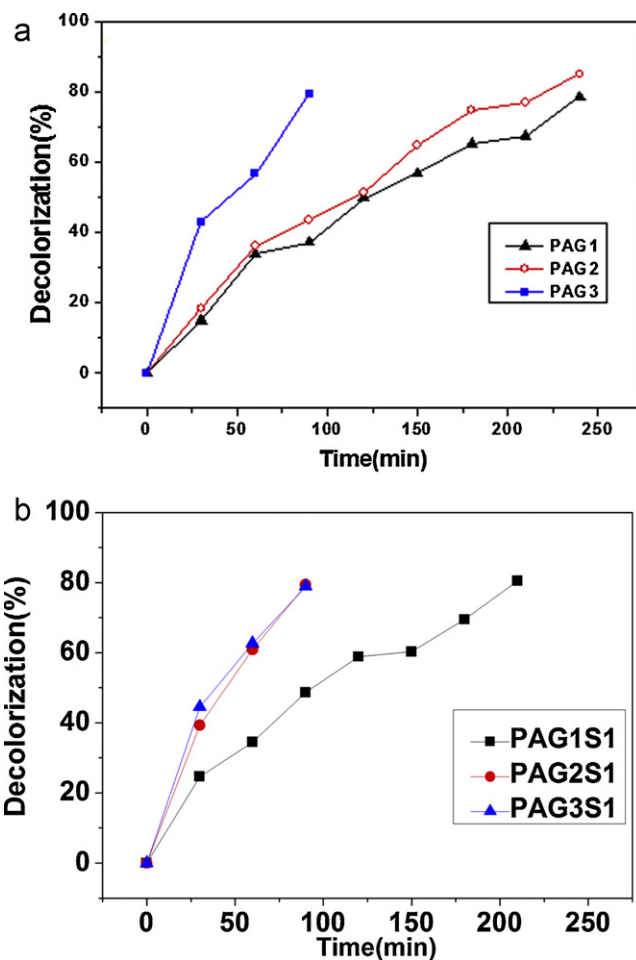$$D_{A\,eff} = \frac{\varepsilon D_{KA}}{\tau} = \frac{\varepsilon (0.67\, r\, \nu)}{\tau}$$

where $D_{A\,eff}$ is the effective diffusivity in a porous medium, ε is the porosity (void fraction), τ is the tortuosity factor, r is the average pore radius, and ν is the average molecular velocity for dye. The diffusion is proportional to the average pore radius and void fraction.

To investigate the potential as a photocatalyst for the current ZnO nanograss pore-array films, we conducted a series of photocatalysis experiments to investigate the effect of catalyst loading and surface morphology. The experiments were performed using PAG1, PAG2, and PAG3 catalystsfor dye solutions of 15 mg/L. The
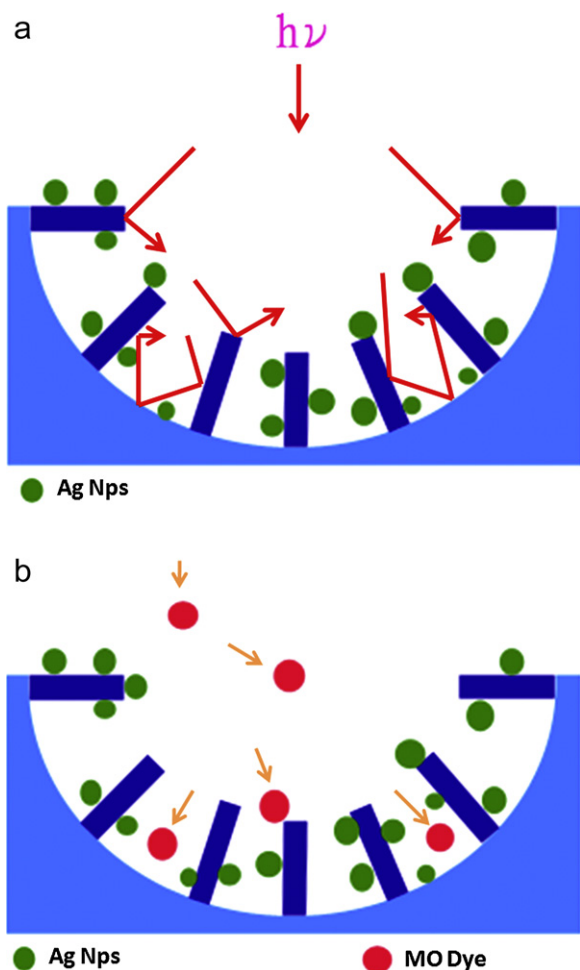
Fig. 8. Schematic illustrations of (a) the interface scattering caused by the porous structure and (b) the diffusion of dye molecules toward the porous nanograss decorated pore-array photocatalysts.

Fig. 9. The decolorization efficiency of (a) nanostructured ZnO photocatalysts with various surface texture and (b) Ag nanoparticles decorated ZnO photocatalysts.

ZnO catalyst loadings for PAG1, PAG2, and PAG3 catalyst are 300, 325, and 375 μg ZnO/cm^2, respectively. The ZnO catalyst loadings of PAGx consisted of the pore-array layers and the nanograss layer. The amounts of ZnO on the pore-array layers of PAGn were about the same. The differences resulted from the amounts of ZnO nanograss layer. The decolorization efficiency for MO at various catalysts loading was depicted in Fig. 9(a). Although the initial slopes of the curve of PAG2 is slightly larger than that of PAG1, the decolorization efficiency of PAG1 is close to that of PAG2. As the nanograss growth time increases, PAG3 exhibits better decolorization efficiency than PAG1 and PAG2 do. With the increase of catalyst loading, total active surface area increases [27]. Maximum decolorization is observed for PAG3. Further increase in the

nanograss growth time (longer than 2 h) leads to the decrease of phocatalysis properties. The pore structure of the pore-array surfaces is completely filled by the nanograss when the nanograss growth time is longer than 2 h. As long as the nanograss growth time is shorter than 2 h, creating nanograss on the pore-array surfaces can generate a three-dimensional hemisphere structure which may have larger surface area than the flat ZnO film and the nanorod film. Such three-dimensional porous morphology may also enhance the diffusion and adsorption of dye in the solution.

The apparent first-order reaction rate constants calculated from the slopes of those curves are shown in Table 2. It demonstrates that the apparent rate constant of the MO photodegradation using the PAG3 film is thirteen times magnitude larger than that using the ZnO nanorod film. The PAG3 film preformed

Table 2
The apparent first-order reaction rate constants for photodegradation of methyl orange and the ZnO and Ag loading of the photocatalyst.

|	ZnO loading (μg/cm^2)			Ag loading (μg/cm^2)	k (h^{-1})
	Pore-array	Nanograss	Total		
PAG1	125	175	300	–	2.75
PAG2	125	200	325	–	3.34
PAG3	125	250	375	–	8.24
PAG1S1	125	175	300	12.5	3.41
PAG2S1	125	200	325	25.0	8.50
PAG3S1	125	250	375	37.5	8.34
Flat film	–	–	225	–	0.05
Nanorod film	–	–	250	–	0.6
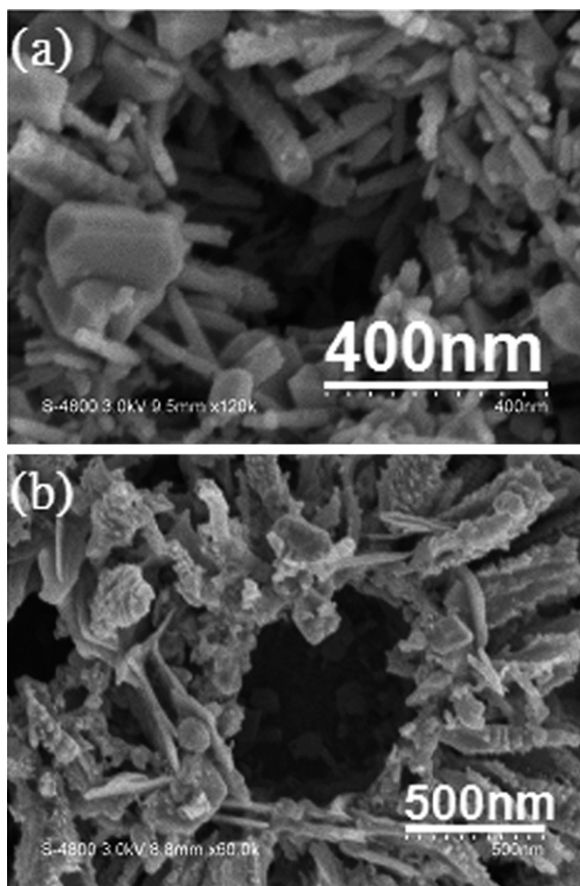
Fig. 10. The FESEM images of the Ag nanoparticles decorated ZnO nanograss pore-array films (a) PAG3S1 and (b) PAG3S3 films with different amount of Ag.

better than PAG1 and PAG2 films. The high photocatalytic property observed for the nanograss decorated pore-array films reveals the advantages of the open porous architecture. Porosity and pore radius can have a large effect on diffusion and adsorption of dye molecules.

3.4.2. Modification by silver nanoparticle

3.4.2.1. Surface morphology of PAGn substrate. Fig. 9(b) shows the decolorization efficiency versus time curves using various Ag nanoparticles modified photocatalysts. MO photodegradation performance of PAG1S1 with Ag nanoparticles on the surface is better than that of PAG1 without Ag nanoparticles decoration. This is mainly a result of the deposited Ag nanoparticles that can facilitate charge separation by attracting the photoexcited electrons of ZnO nanostructure, thus providing more electrons for the decoloration of MO.
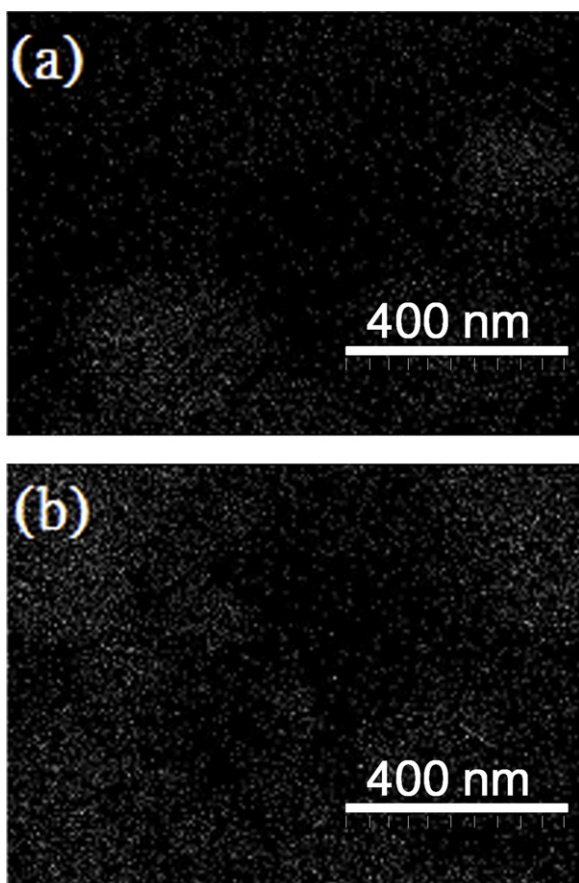
The apparent rate constant of the MO photodegradation using the PAG2S1 catalyst is about 2.5 times of that using the PAG2 catalyst. The separated nanograss surrounded by the MO solution would enhance the charge separation and thus reduce the recombination of the photogenerated electrons and holes. Rapid transfer of the charge carriers to the solution-phase redox couples to prevent from the electron–hole pairs recombination is usually required to enhance the overall photocatalytic efficiency. Silver nanoparticles were deposited on the ZnO nanograss decorated pore-array photocatalysts to facilitate electron transfer out of the conduction band of the ZnO semiconductor after UV irradiation. Interfacial charge transfer can be enhanced by the silver nanoparticles which act as the sink for photoinduced charge carriers. Subramanian et al. [28] found that metal–semiconductor composites exhibit shift in
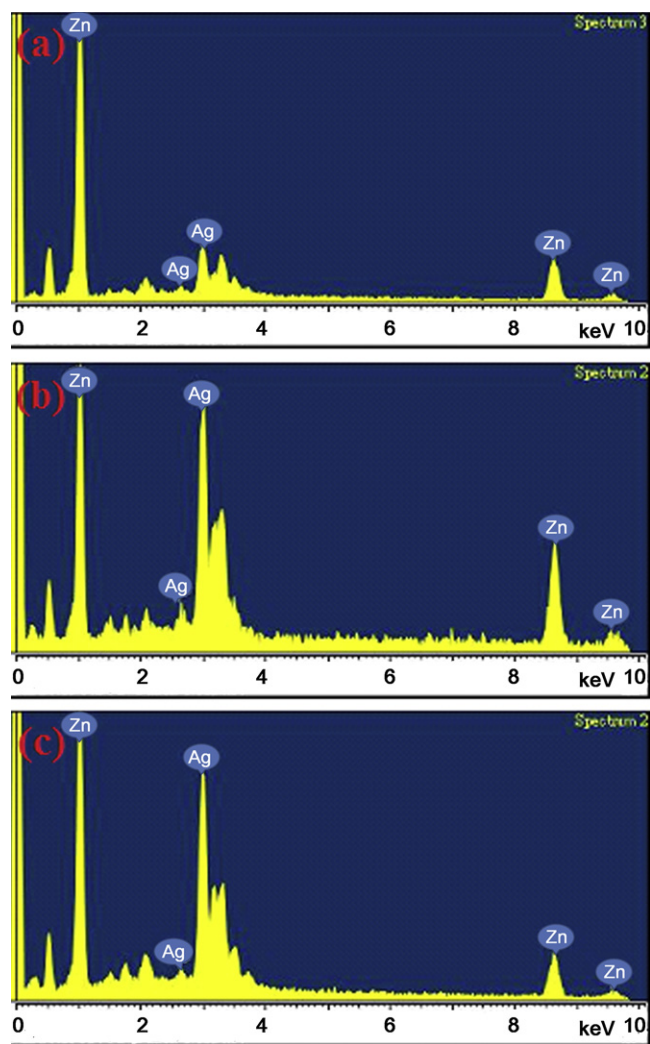
Fig. 11. The FESEM energy dispersive spectroscopy of the Ag nanoparticles decorated ZnO nanograss pore-array films (a) PAG3S1, (b) PAG3S2, and (c) PAG3S3 with different amount of Ag nanoparticles.

the Fermi level to more negative potential. Such shift results in the enhancement of the efficiency of interfacial charge-transfer process. Wu reported that the noble metal acted as a sink for photoinduced charge carriers, promoting interfacial charge transfer processes [29]. However, the photodegradation performance of PAG3S1 and PAG3 are about the same. As shown in Fig. 3, the diameter of the pore became smaller as the nanograss growth time got longer. PAG3 consists of hemisphere pores with small openings (D) at the top. Decorating Ag nanoparticles on the PAG3 surface may result in three kinds of changes. One is the decrease of the active photodegradation sites. The second is the decrease of D. The third is the enhanced electron transfer out of the conduction band of the ZnO semiconductor after UV irradiation. The third helps to enhance the photodegradation performance, while the other two changes lower the photodegradation performance. PAG3 exhibits a better photodegradation performance than PAG1 and PAG2. Because of the compromise between the above-mentioned opposite effects, PAG3S1 did not show better photodegradation performance than PAG3 after the modification by Ag nanoparticles. The apparent rate constant of the MO photodegradation using the PAG2S1 catalyst is about 2.5 times of that using the PAG1S1 catalyst. The increase of the apparent rate constant obviously is attributed to the surface increase for the charge carriers reacting with the species in the solution.
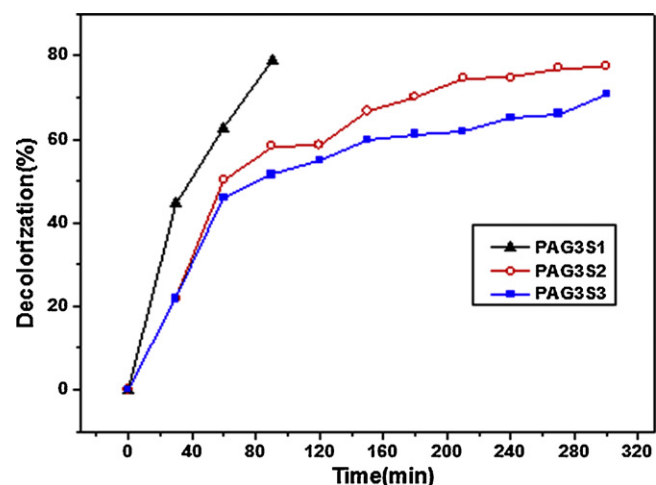
Fig. 12. The SEM/EDX Ag-mapping of the Ag nanoparticles decorated ZnO nanograss pore-array films (a) PAG3S1 and (b) PAG3S3.

Fig. 13. The decolorization efficiency of the Ag nanoparticles decorated ZnO nanograss pore-array films with various amounts of Ag nanoparticles.

exceeds 5×10^{-3} mol/L, the amounts of decorated Ag nanoparticles on PAG3S2 and PAG3S3 films remain nearly the same.

Fig. 12 shows the SEM/EDX Ag-mapping of the Ag decorated ZnO nanograss pore-array films (a) PAG3S1 and PAG3S3 by energy dispersive spectroscopy analysis. The location of Ag element is an indication of the distribution of Ag nanoparticles on the ZnO nanograss pore-array surfaces. For the PAG1S1 film, some regions with high density of the bright spots were found. The rest region exhibited bright spots with lower density. The high spot-density area of the PAG3S3 film is larger than that of the PAG3S1 film. The amount of silver nanoparticles deposited on the PAG3S3 film is more than that of the PAG3S1 film.

Fig. 13 shows the decolorization efficiency of PAG3S1, PAG3S2, and PAG3S3 films with various amounts of Ag nanoparticles. Comparing the photodegradation efficiency of PAG3S1 catalyst, further increase in the concentration of Ag for PAG3S2 and PAG3S3 catalysts leads to a depressed efficiency of MO photodegradation. The excess amount of Ag may cover a large part of ZnO surfaces, which in turn decreases the number of active sites for photocatalysis. The high coverage of Ag may also retard the access of UV irradiation to ZnO surfaces, resulting in a reduced amount of photoexcited charge carriers and decreased photocatalytic performance. Similar result was found in the gold nanopaarticles decorated TiO_2 thin-film photocatalysts [30]. Moreover, as the concentration of Ag increased, the catalyst was surrounded by more and more Ag nanoparticles which tended to aggregate, as observed in Fig. 9b. These aggregated metal nanoparticles may act as an electron–hole recombination center rather than the electron trapper [31,32]. It leads to the depression of photocatalytic efficiency. In addition, the intensity of the incident irradiation on ZnO nanograss will be reduced by scattering due to the larger Ag aggregates.

4. Conclusions

ZnO pore-array photocatalysts with the wide round opening at the top and nanograss decorated hemisphere bottom have been developed in this study. The active surface area of the catalyst increases when the length of ZnO nanograss increases. The diffusion of dye molecules around the catalyst can be enhanced. Strongly scattering surfaces randomize the direction of light internally within the photocatalyst and increase the effective absorption in the photocatalyst. The photodegradation of MO is enhanced when the Ag nanoparticles are deposited on the ZnO nanograss. The photocatalytic activities are dependent on the size and density of the loaded Ag nanoparticles. The amount of Ag nanoparticles should

3.4.2.2. Precursor concentration. To demonstrate the effect of amount of deposited Ag nanoparticles on the photocatalytic efficiency for the Ag nanoparticles decorated ZnO nanograss pore-array films, further comparative experiments were conducted. Three photocatalysts (PAG3S1, PAG3S2, and) which were prepared by different precursor ($AgNO_3$) concentration (10^{-3}, 5×10^{-3}, 10^{-2} M) were used for MO photodegradation. Fig. 10 shows the SEM images of the Ag nanoparticles decorated ZnO nanograss pore-array (a) PAG3S1 and PAG3S3 films with different amountsof Ag. The density of the nanoparticles deposited on the ZnO nanorods increased with increasing the $AgNO_3$ concentration. Fig. 10b reveals that there are large Ag aggregates formed on the surface of the ZnO nanograss. The diameters and densities of the Ag nanoparticles formed by this photocatalytic deposition method on the surface of the ZnO nanograss are tunable through varying the $AgNO_3$ concentration.

The energy-dispersive spectra were measured to compare the amount of Ag nanoparticles on the photocatalyst. Fig. 11 shows the SEM energy dispersive spectroscopy of (a) PAG3S1 (b) PAG3S2, and (c) PAG3S3 films with different amount of Ag. The height of Ag peak increases when the precursor concentration increases. From the energy-dispersive spectra, the mole ratios of Ag to ZnO for the films (PAG3S1, PAG3S2, and PAG3S3) prepared with different concentrations of Ag^+ (10^{-3}, 5×10^{-3}, and 10^{-2} mol/L) were 0.17 (14.5/85.5), 0.616 (38.1/61.9), and 0.597 (37.4/62.6), respectively. The amount of Ag nanoparticles decorated on the ZnO nanograss pore-array films increased with increasing concentration of Ag^+ ions. More silver nanoparticles formed on the surface of nanograss decorated pore-array. But when the concentration of Ag^+ ions

be optimized to prevent aggregations of Ag nanoparticles and sharp decrease of the active photodegradation sites. These characteristics thus offer the potential for gaining high performances even with immobilized ZnO photocatalysts. The deposition of Ag nanoparticles on the photocatalyst surface and the modification of surface texture which determines the catalyst surface to reactor volume ratio can not only solve the problems of powder photocatalysts recovery and recycling, but also improves in the photocatalytic efficiency of the immobilized photocatalysts.

Acknowledgements

References

[1] A. Akyol, M. Bayramoglu, Preparation and characterization of supported ZnO photocatalyst by zincate method, J. Hazard. Mater. 175 (2010) 484–491.
[2] Z. Li, W. Shen, W. He, X. Zu, Effect of Fe-doped TiO_2 nanoparticle derived from modified hydrothermal process on the photocatalytic degradation performance on methylene blue, J. Hazard. Mater. 155 (2008) 590–594.
[3] H.C. Yatmaz, A. Akyol, M. Bayramoglu, Kinetics of the photocatalytic decolorization of an azo reactive dye in aqueous ZnO suspensions, Ind. Eng. Chem. Res. 43 (2004) 6035–6039.
[4] I.M. Arabatzis, T. Stergiopoulos, M.C. Bernard, D. Labou, S.G. Neophytides, P. Falaras, Silver-modified titanium dioxide thin films for efficient photodegradation of methyl orange, Appl. Catal. B: Environ. 42 (2003) 187–201.
[5] M.V. Diamanti, M. Ormellese, E. Marin, A. Lanzutti, A. Mele, M.P. Pedeferri, Anodic Titanium oxide as immobilized photocatalyst in UV or visible light devices, J. Hazard. Mater. 186 (2011) 2103–2109.
[6] V. Kandavelu, H. Kastien, K.R. Thampi, Photocatalytic degradation of isothiazolin-3-ones in water and emulsion paints containing nanocrystalline TiO_2 and ZnO catalysts, Appl. Catal. B: Environ. 48 (2004) 101–111.
[7] T.A. Egerton, I.R. Tooley, Effect of changes in TiO_2 dispersion on its measured photocatalytic activity, J. Phys. Chem. B 108 (2004) 5066–5072.
[8] F. Sun, W. Cai, Y. Li, B. Cao, Y. Lei, L. Zhang, Morphology-controlled growth of large-area two-dimensional ordered pore-arrays, Adv. Funct. Mater. 14 (2004) 283–288.
[9] C.J. Chang, S.T. Hung, Electrochemical deposition of ZnO pore-array structures and photoconductivity of ZnO/polymer hybrid films, Thin Solid Films 517 (2008) 1279–1283.
[10] F. Sun, W.P. Cai, Y. Li, B. Cao, F. Lu, G. Duan, L. Zhang, Morphology control and transferability of ordered through-pore-arrays based on the electrodeposition of a colloidal monolayer, Adv. Mater. 16 (2004) 1116–1121.
[11] C.J. Chang, E.H. Kuo, Light-trapping effects and dye adsorption of ZnO hemisphere-array surface containing growth-hindered nanorods, Colloid Surf. A 363 (2010) 22–29.
[12] Y. Li, W. Cai, G. Duan, B. Cao, F. Sun, F. Lu, Superhydrophobicity of 2D ZnO ordered pore-arrays formed by solution-dipping template method, J. Colloid Interf. Sci. 287 (2005) 634–639.
[13] C.J. Chang, S.T. Hung, Wettability control of micropore-array films by altering the surface nanostructures, J. Nanosci. Nanotechnol. 10 (2010) 4674–4678.
[14] C.J. Chang, E.H. Kuo, Roughness-enhanced thermal-responsive surfaces by surface-initiated polymerization of polymer on ordered ZnO pore-array films, Thin Solid Films 519 (2010) 1755–1760.
[15] S.I. Matsushita, T. Miwa, D.A. Tryk, A. Fujishima, New mesostructured porous TiO_2 surface prepared using a two-dimensional array-based template of silica particles, Langmuir 14 (1998) 6441–6447.
[16] E. Yablonovitch, T.J. Gmitter, R.D. Meade, A.M. Rappe, K.D. Brommer, J.D. Joannopoulos, Donor and acceptor modes in photonic band structure, Phys. Rev. Lett. 67 (1991) 3380.
[17] C.D. Elizabeth, K.V. Oomman, G.O. Keat, Sensors 2 (2002) 91.
[18] M. Imada, S. Noda, A. Chutinan, T. Tokuda, M. Murata, G. Sasaki, Coherent two-dimensional lasing action in surface-emitting laser with triangular-lattice photonic crystal structure, Appl. Phys. Lett. 75 (1999) 316–318.
[19] S. Ikeda, N. Sugiyama, B. Pal, G. Marci, L. Palmisano, H. Noguchi, K. Uosaki, B. Ohtani, Photocatalytic activity of transition-metal-loaded titanium(IV) oxide powders suspended in aqueous solutions: correlation with electron–hole recombination kinetics, Phys. Chem. Chem. Phys. 3 (2001) 267–273.
[20] S. Hotchandani, P.V. Kamat, Charge–transfer processes in coupled semiconductor systems. Photochemistry and photoelectrochemistry of the colloidal cadmium sulfide–zinc oxide system, J. Phys. Chem. 96 (1992) 6834–6839.
[21] H. Zeng, P. Liu, W. Cai, S. Yang, X. Xu, Controllable Pt/ZnO porous nanocages with improved photocatalytic activity, J. Phys. Chem. C 112 (2008) 19620–19624.
[22] L. Sun, J. Li, C. Wang, S. Li, Y. Lai, H. Chen, C. Lin, Ultrasound aided photochemical synthesis of Ag loaded TiO_2 nanotube arrays to enhance photocatalytic activity, J. Hazard. Mater. 171 (2009) 1045–1050.
[23] A.V. Rupa, D. Manikandan, D. Divakar, T. Sivakumar, Effect of deposition of Ag on TiO_2 nanoparticles on the photodegradation of reactive yellow-17, J. Hazard. Mater. 147 (2007) 906–913.
[24] C.J. Chang, M.S. Wu, P.C. Kao, Morphology and properties of low dielectric constant polymeric films with electrophoresis induced gradient close-pores distribution, Micropor. Mesopor. Mater. 111 (2008) 267–275.
[25] M. Berginski, J. Hupkes, M. Schulte, G. Schope, H. Stiebig, B. Rech, M. Wuttig, The effect of front ZnO:Al surface texture and optical transparency on efficient light trapping in silicon thin-film solar cells, J. Appl. Phys. 101 (2007) 074903–074911.
[26] C.J. Geankoplis, Transport Processes and Separation Process Principles, 4th edition, Pearson Education, Inc., 2003, pp. 0–505.
[27] M.S.T. Gongalves, A.M.F. Oliveira-Campos, E.M.M.S. Pinto, P.M.S. Plasjncia, M.J.R.P. Queiroz, Photochemical treatment of solutions of azo dyes containing TiO_2, Chemosphere 39 (1999) 781–786.
[28] V. Subramanian, E.E. Wolf, P.V. Kamat, Catalysis with TiO_2/gold nanocomposites. Effect of metal particle size on the Fermi level equilibration, J. Am. Chem. Soc. 126 (2004) 4943–4950.
[29] J.J. Wu, C.H. Tseng, Photocatalytic properties of nc–Au/ZnO nanorod composites, Catal. B: Environ. 66 (2006) 51–57.
[30] I.M. Arabatzis, T. Stergiopoulos, D. Andreeva, S. Kitova, S.G. Neophytides, P. Falaras, Characterization and photocatalytic activity of Au/TiO_2 thin films for azo-dye degradation, J. Catal. 220 (2003) 127–135.
[31] W. Lu, S. Gao, J. Wang, One-pot synthesis of Ag/ZnO self-assembled 3D hollow microspheres with enhanced photocatalytic performance, J. Phys. Chem. C 112 (2008) 16792–16800.
[32] W.T. Chen, Y.J. Hsu, L-Cysteine-assisted growth of core–satellite ZnS–Au nanoassemblies with high photocatalytic efficiency, Langmuir 26 (2009) 5918–5925.